Available online at www.sciencedirect.com
SCIENCE DIRECT®
Physics and Chemistry of the Earth 29 (2004) 225–240
PHYSICS and CHEMISTRY of the EARTH
www.elsevier.com/locate/pce

Sensitivity of GNSS radio occultation data to horizontal variability in the troposphere

Ulrich Foelsche *, Gottfried Kirchengast

Institute for Geophysics, Astrophysics, and Meteorology (IGAM), University of Graz, Universitätsplatz 5, A-8010 Graz, Austria

Abstract

We addressed the sensitivity of Global Navigation Satellite System (GNSS) radio occultation (RO) measurements to atmospheric horizontal variability based on realistically simulated data. Retrieved parameters from refractivity via pressure, and geopotential height to dry temperature were investigated. The errors in a realistic horizontally variable atmosphere relative to errors in a spherically symmetric atmosphere were quantified based on an ensemble of 60 occultation events. These events have been simulated using ray tracing through a representative European Centre for Medium-Range Weather Forecasts (ECMWF) T213L50 analysis field with and without horizontal variability, respectively. Below ~7 km height biases and standard deviations of all parameters under spherical symmetry are significantly smaller than corresponding errors in a realistic atmosphere with horizontal variability. The relevance of the geometry of reference profiles was assessed in this context as well. A significant part of the total error below ~7 km can be attributed to adopting reference profiles vertically at mean tangent point locations instead of extracting them along actual 3D tangent point trajectories. The sensitivity of retrieval products to the angle-of-incidence of occultation rays relative to the boresight direction of the receiving antenna was analyzed for three different azimuth sectors (0–10°, 20–30°, 40–50°) with 20 events in each sector. Below about 7 km, most errors were found to increase with increasing angle of incidence. Dry temperature biases between 7 and 20 km exhibit no relevant increase with increasing angle of incidence, which is favorable regarding the climate monitoring utility of the data.

Keywords: Remote sensing; Atmospheric propagation; Inverse theory; Pressure, density, and temperature

1. Introduction

A detailed description of the Global Navigation Satellite System (GNSS) radio occultation (RO) technique and estimates of errors in the troposphere caused by horizontal variation can be found in Kursinski et al. (1997). Ahmad and Tyler (1999) performed an analytical approach to the errors introduced by refractivity gradients. The simulation study by Healy (2001) focused on bending angle and impact parameter errors caused by horizontal refractivity gradients in the troposphere.

1.1. Study objectives

We investigated the sensitivity of atmospheric profiles retrieved from Global Navigation Satellite System (GNSS) RO data to atmospheric horizontal variability in a twofold manner: first, the errors in a (realistic) horizontally variable atmosphere are compared with errors in a spherically symmetric atmosphere, based on an ensemble of 60 occultation events (using an European Centre for Medium-Range Weather Forecasts, ECMWF, T213L50 analysis field with and without horizontal variability). The difference incurred by either assuming the ''true'' profile vertically at a mean event location (the common practice) or more precisely along the estimated 3D tangent point trajectory traced out during the event was assessed in this context as well. Second, the sensitivity of retrieval products to the angle-of-incidence of occultation rays relative to the boresight direction of the receiving antenna (aligned with the LEO orbit plane) was analyzed based on ensembles of events (from the same ECMWF analysis field) for three different angle-of-incidence classes (±10°, ±20° to ±30°, ±40° to ±50°). This provided important insights into how much the climate monitoring utility of GNSS occultation data depends on occultation event geometry.

* Corresponding author. Tel.: +43-316-380-8590; fax: +43-316-380-9825.
E-mail address: ulrich.foelsche@uni-graz.at (U. Foelsche).

1474-7065/$ - see front matter © 2004 Elsevier Ltd. All rights reserved.
doi:10.1016/j.pce.2004.01.007

1.2. Study overview

The EGOPS software tool (End-to-end GNSS Occultation Performance Simulator, version 4.0) was used to generate realistically simulated measurements of the observables refractivity, total atmospheric pressure, geopotential height, and (dry) temperature. For a detailed description of EGOPS (see Kirchengast, 1998; Kirchengast et al., 2001). Section 2 gives an overview on the experimental setup. Results on the sensitivity to horizontal variability are presented in Section 3, the results on sensitivity to angle-of-incidence are shown and discussed in Section 4. Conclusions and an outlook are finally provided in Section 5.

2. Experimental setup

2.1. Geometry

We assumed a full constellation of 24 Global Positioning System (GPS) satellites as transmitters and a GNSS Receiver for Atmospheric Sounding (GRAS) sensor onboard the METOP satellite (nominal orbit altitude ~830 km). With such a constellation a total of somewhat over 500 rising and setting occultation events per day can be obtained during a simulation over a 24 h period. The simulated day was September 15, 1999, the date of the ECMWF analysis field used in the forward modeling.

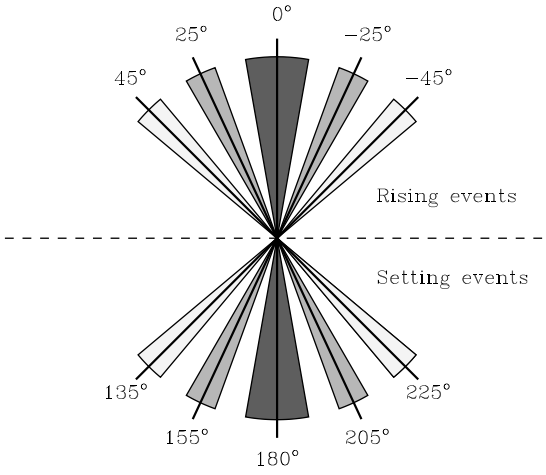

Fig. 1. Schematic illustration of azimuth sectors used in the study: sector 1 (dark gray), sector 2 (medium gray), and sector 3 (light gray). Rising events are observed with the antenna oriented in flight direction (0° azimuth), setting events with the aft-looking antenna.

We collected occultation events in three different azimuth sectors relative to the boresight direction of the receiving antennae. A schematic illustration of this division into several "angle-of-incidence" sectors is given in Fig. 1, while Table 1 summarizes the simulation design in terms of numbers of events simulated per sub-sector defined. Sector 1 (dark gray in Fig. 1) comprises azimuth angles between −10° and +10° (rising occultations) plus angles between 170° and 190° (setting occultations). Angles of incidence in the range of $|25°| \pm 5°$, symmetric to the orbit plane, compose Sector 2 (four medium gray sub-sectors in Fig. 1). Sector 3 corresponds to angles of incidence in the range of $|45°| \pm 5°$, symmetric to the orbit plane (light gray in Fig. 1).

With restriction to the described azimuth sectors we obtained a total of 321 occultation events during the selected 24 h period. The geographic distribution is shown in the top panel of Fig. 2. From this sample of 321 occultations we selected 20 events per azimuth sector (60 events in total) in order to keep computational expenses limited. Selection criteria were:

- Uniform distribution in latitude an longitude in each sector.
- Equal density over oceans and over continents in each sector.
- Same amount of rising and setting occultations (see Table 1).

The geographic distribution of the 60 selected occultation events is displayed in the bottom panel of Fig. 2. It is visible that a reasonably representative coverage is achieved with the selected ensemble.

2.2. Forward modeling

High resolution (T213L50) analysis fields from the European Centre for Medium-Range Weather Forecasts (ECMWF) for September 15, 1999, 12 UT, were used to

Table 1
Azimuth sectors used in this study

	Sector 1	Sector 2	Sector 3	No. of events
Rising events	0° to −10°	−20° to −30°	−40° to −50°	15
	0° to +10°	+20° to +30°	+40° to 50°	15
Setting events	170° to 180°	150° to 160°	130° to 140°	15
	180° to 190°	200° to 210°	220° to 230°	15
No. of events	20	20	20	60

We selected 5 rising or 5 setting events, respectively, in each of the 12 sub-sectors, leading to a total ensemble of 60 events.

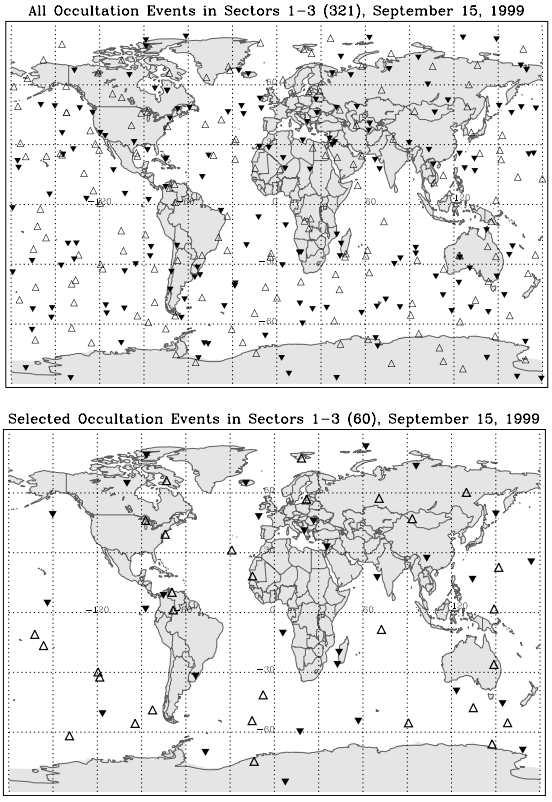

Fig. 2. Locations of occultation events during one day in all three azimuth sectors. Top panel: all events, bottom panel: selected events (20 in each sector). Upright open triangles denote rising occultations. Upside-down filled triangles denote setting occultations.

generate realistic atmospheric phase delays. The horizontal resolution (T213) corresponds to 320 times 640 points in latitude and longitude, respectively, and thus furnishes several grid points within the typical horizontal resolution of an occultation event of ~300 km (e.g., Kursinski et al., 1997). This dense sampling is important to have a sufficient representation of horizontal variability errors in occultation measurements. In the vertical, 50 levels (L50, hybrid pressure coordinates) extend from the surface to 0.1 hPa, being most closely spaced in the troposphere, which represents good vertical sampling. In order to illustrate the resolution of the T213L50 field utilized, slices of specific humidity and temperature are displayed in Fig. 3.

The MSIS climatological model (Hedin, 1991) was used, with a smooth transition from the ECMWF analysis field upwards, above the vertical domain of that field. As we focused on the troposphere, we made the reasonable assumption that ionospheric residual errors can be neglected (Steiner et al., 1999). Forward modeling was therefore employed without ionosphere, which corresponds to considerable savings in computational expenses.

We performed high-precision 3D ray tracing with sub-millimetric accuracy and a sampling rate of 10 Hz for all forward modeled events through the ECMWF analysis. In order to be able to compare the ensemble of measurements subjected to horizontal variability with one without horizontal variability, two separate ensembles of 60 events were forward modeled: one with employing the analysis field with its 3D structure as is, the other with artificially enforcing spherical symmetry for all events. The latter case was obtained by applying the atmospheric profile at the mean tangent point of an occultation event over the entire domain probed.

As in the real atmosphere, occultation events over oceans at low latitudes occasionally failed to penetrate the lowest ~4 km of the troposphere. In the present simulations, the reason is that the ray tracer encounters super-refractive structures, which it cannot "overcome". All 60 events included in the final ensemble and used for computing the statistical results reached to a minimum height of ~2 km or closer to the surface. The retrieval processing (Section 2.3) led, for individual events, to a further increase of the minimum height reached.

2.3. Observation system modeling and retrieval processing

Realistic errors (including error sources like orbit uncertainties, receiver noise, local multipath errors and clock errors) have been superimposed on the obtained simulated phase measurements. For this realistic receiving system simulation, we reflected (conservatively) the specifications and error characteristics of the GRAS instrument (e.g., GRAS-SAG, 1998).

Regarding retrieval processing, we applied a geometric optics bending angle retrieval scheme, more specifically, the "enhanced bending angle retrieval" algorithm of EGOPS. The core of this algorithm, transforming phase delays to bending angles, is the algorithm described by Syndergaard (1999), which was enhanced to include inverse covariance weighted statistical optimization (with prior best-fit a priori profile search) as described by Gobiet and Kirchengast (2002). Since Forward Modeling has been performed without ionosphere, ionospheric correction could be omitted.

Refractivity profiles have been computed using a standard Abel transform retrieval employing the EGOPS-internal algorithm of Syndergaard (1999). Profiles of total atmospheric pressure and temperature, respectively, have been obtained using a standard dry air retrieval algorithm as again developed by Syndergaard (1999). Geopotential height profiles where obtained by converting geometrical heights z of pressure levels via the standard relation $\mathrm{d}Z = (g(z,\varphi)/g_0)\mathrm{d}z$ (e.g., Salby, 1996) to geopotential heights Z, where $g(z,\varphi)$ invokes the international gravity formula (e.g., Kahle, 1984) and $g_0 = 9.80665\ \mathrm{ms}^{-2}$ is the standard acceleration of gravity. We did not undertake to separately analyze temperature and humidity, since for this baseline analysis

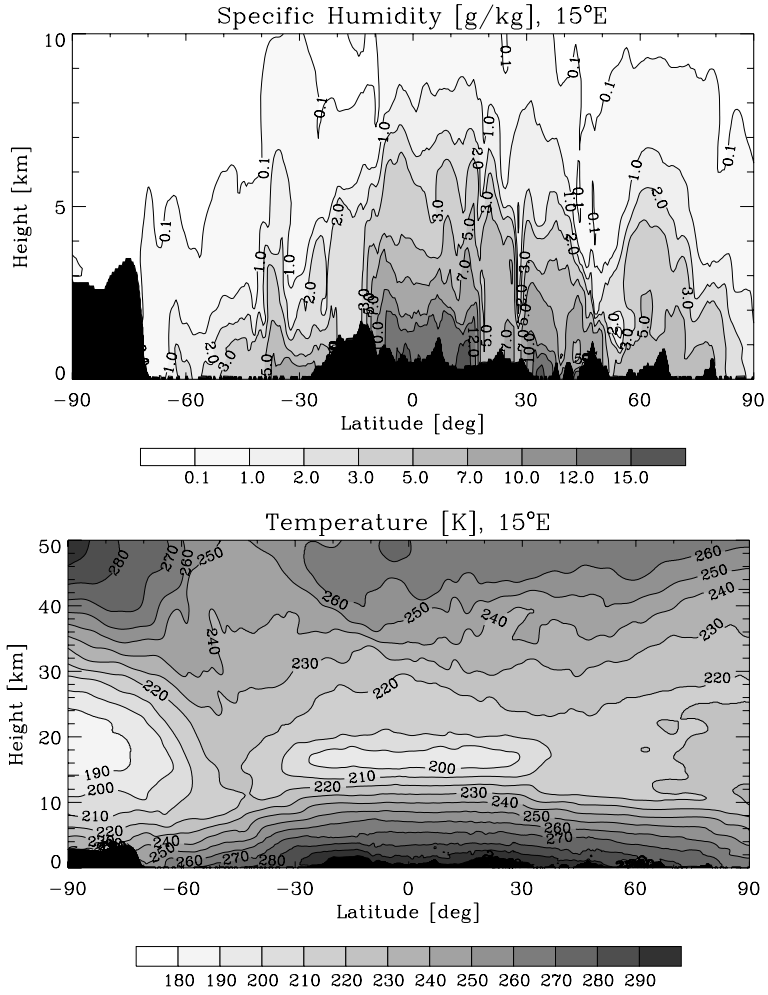

Fig. 3. Atmospheric parameters as functions of latitude and height above the ellipsoid at 15° eastern longitude, September 15, 1999, 12 UT (T213L50 ECMWF analysis field). Top panel: specific humidity in [g/kg], bottom panel (different height range): temperature in [K]. Black regions indicate the orography.

of horizontal variability errors we decided to inspect variables such as refractivity and dry temperature, which do not have mixed in any prior information.

2.4. Reference profiles

For the results shown in Sections 3 and 4, all the retrieved profiles of refractivity, pressure, geopotential height, and temperature, respectively, have been differenced against the corresponding "true" ECMWF vertical profiles at mean tangent point locations, also termed reference profiles. The differences incurred by either assuming the reference profile vertically at a mean event location or along the estimated 3D tangent point trajectory traced out during the event has been assessed as well (within Section 3).

As described in Section 2.3, pressure and temperature profiles were computed, assuming a dry atmosphere, based on standard formulae (Syndergaard, 1999). We consequently compare to "true" (dry) pressure, (dry) geopotential height, and dry temperature profiles from the ECMWF field. This implies that the temperature profiles have increasingly subsumed moisture effects below 10 km. The dependence of dry temperature on actual temperature and humidity is accurately known via the refractivity formula (Smith and Weintraub, 1953), however, so that one can always determine the influence of moisture if desired.

3. Sensitivity to horizontal variability

In this part of the study we focused on the influence of horizontal variability. Results for the "real" atmosphere with horizontal variability are therefore compared with the results for the artificial spherically symmetric atmosphere (upper and middle panels of Figs. 4–7). Furthermore, differences between "true" vertical profiles and "true" profiles extracted along the 3D tangent point trajectories (the latter taken as refer-

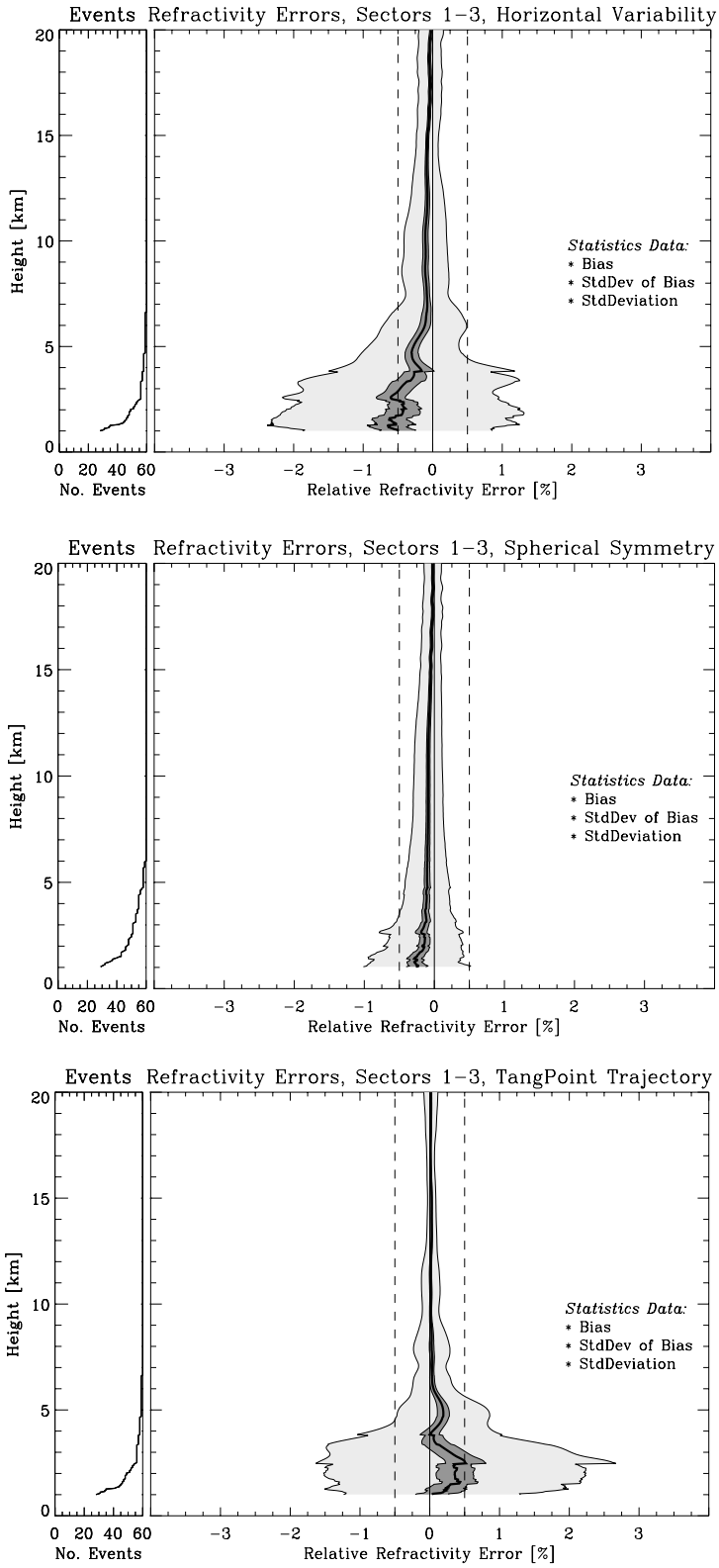

Fig. 4. Refractivity error statistics for the ensemble of all 60 occultation events in all sectors. Top panel: atmosphere with horizontal variability; middle panel: atmosphere with spherical symmetry applied; bottom panel: vertical profile at mean tangent point minus profile along 3D tangent point trajectory.

ence) are shown (bottom panels of Figs. 4–7). The results for the full ensemble of 60 events are illustrated in all panels. The gradual decrease in the number of events towards lower tropospheric levels (small left-hand-side

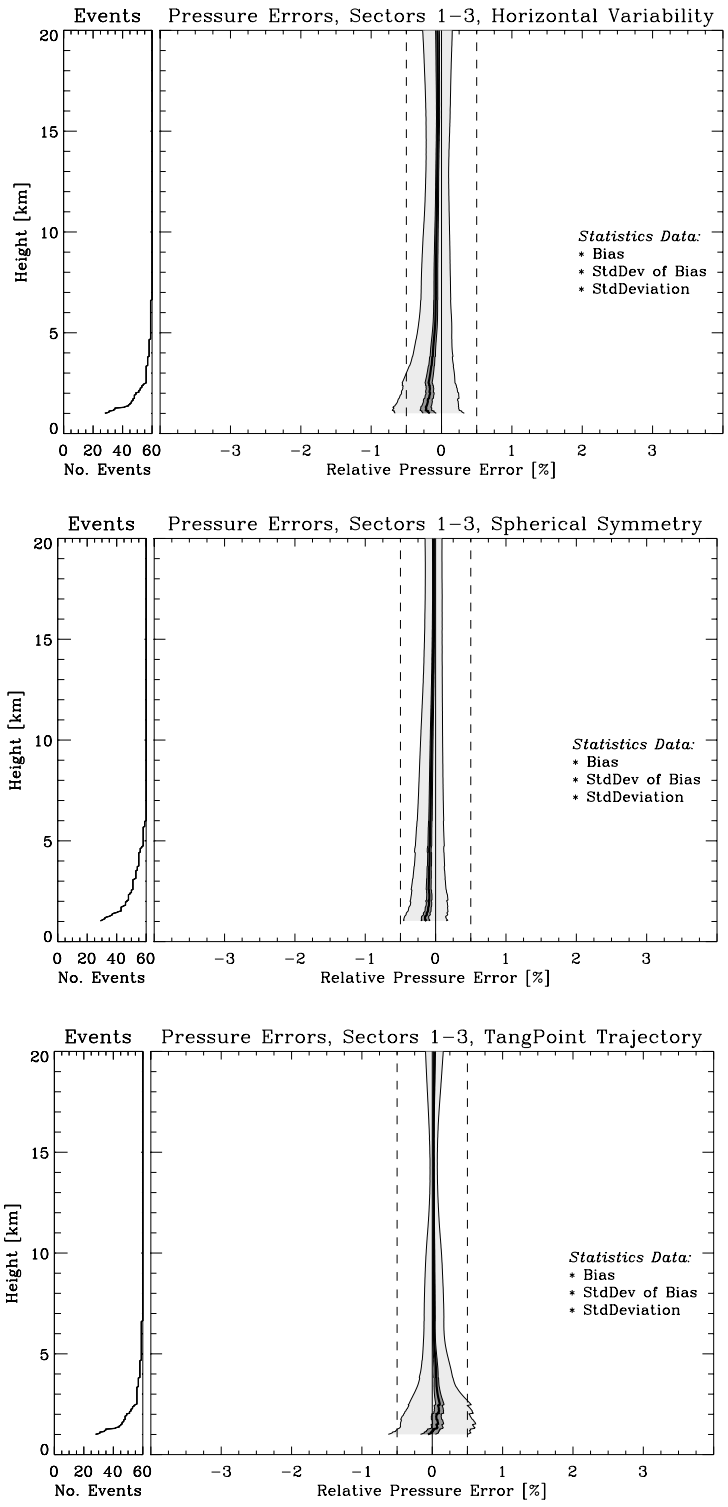

Fig. 5. Pressure error statistics for the ensemble of all 60 occultation events in all sectors. Top panel: atmosphere with horizontal variability; middle panel: atmosphere with spherical symmetry applied; bottom panel: vertical profile at mean tangent point minus profile along 3D tangent point trajectory.

subpanels) is due to the different minimum heights reached by individual events.

Differencing of retrieved profiles with co-located reference profiles allows computation of the total bias errors and standard deviations in the parameters under investigation. The exponential decrease of refractivity and pressure with height inhibits the visual representation of absolute errors. Errors in refractivity

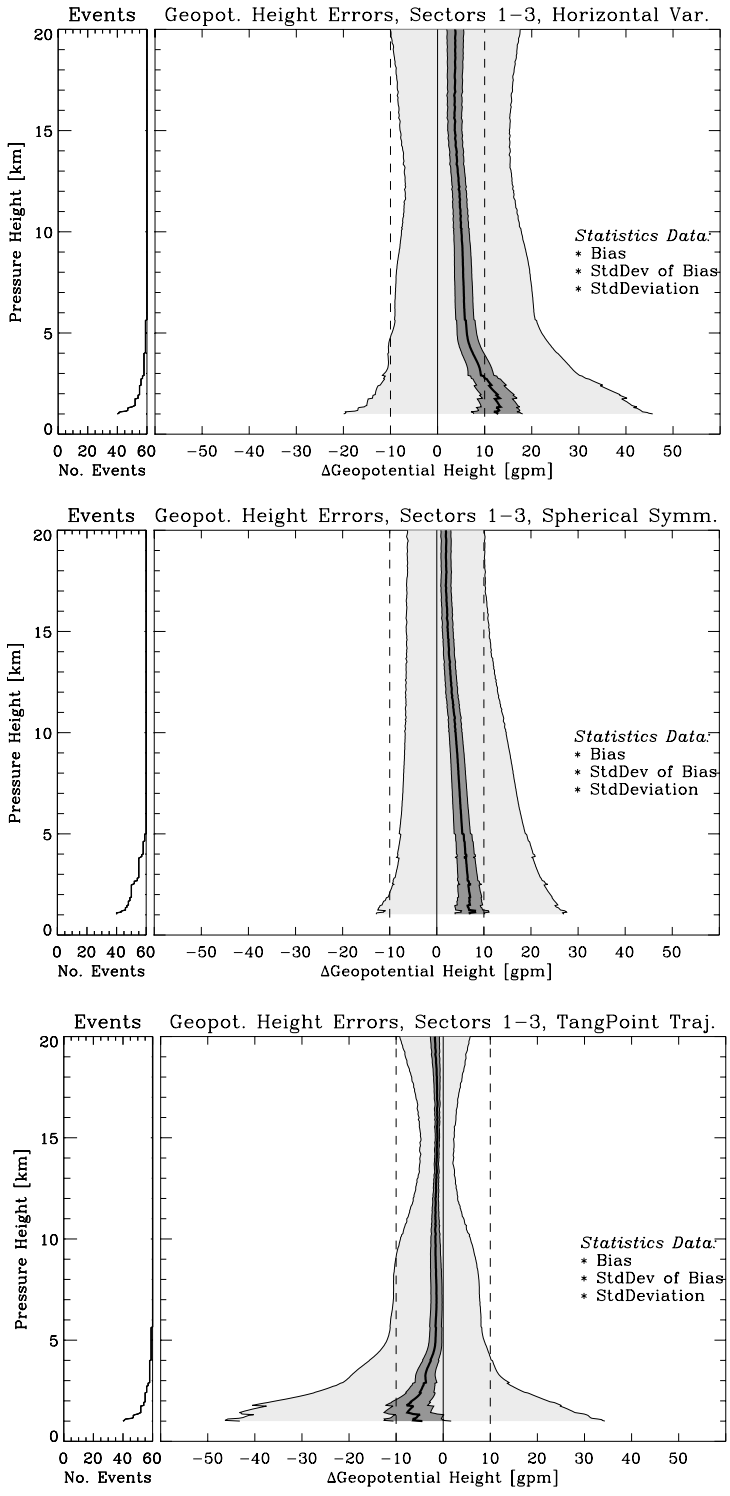

Fig. 6. Geopotential height error statistics for the ensemble of all 60 occultation events in all sectors. Top panel: atmosphere with horizontal variability; middle panel: atmosphere with spherical symmetry applied; bottom panel: vertical profile at mean tangent point minus profile along 3D tangent point trajectory.

(Fig. 4) and pressure (Fig. 5) are thus shown as relative errors in units [%], while geopotential height (Fig. 6) and dry temperature errors (Fig. 7) are displayed in units [gpm] and [K], respectively. All statistics are shown between 1 km and 20 km above (ellipsoidal) surface; dashed vertical lines mark relative errors of 0.5% and absolute errors of 10 gpm and 1 K, respectively.

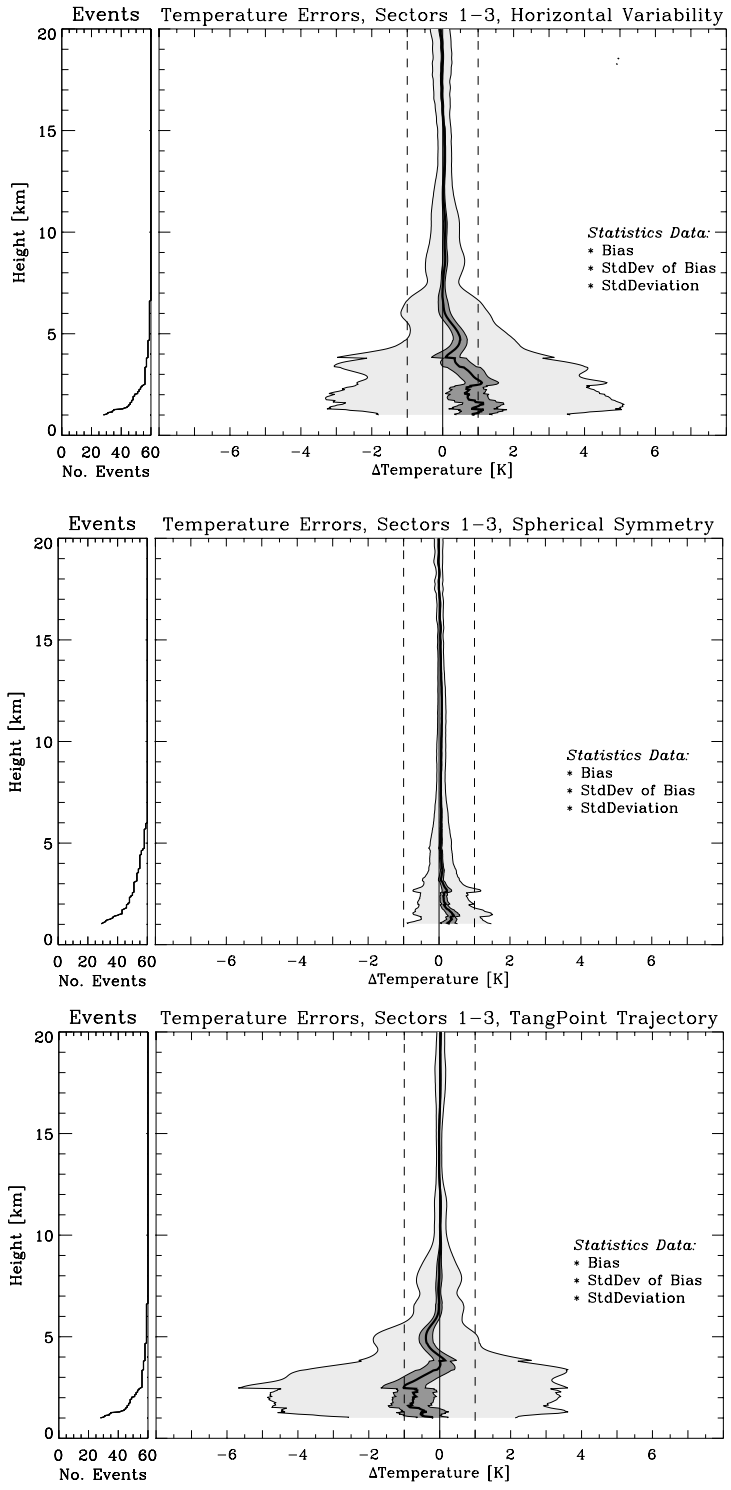

Fig. 7. Temperature error statistics for the ensemble of all 60 occultation events in all sectors. Top panel: atmosphere with horizontal variability; middle panel: atmosphere with spherical symmetry applied; bottom panel: vertical profile at mean tangent point minus profile along 3D tangent point trajectory.

3.1. Refractivity errors

Fig. 4 illustrates that refractivity errors in a horizontally variable atmosphere increase considerably below a height of about 7 km (top panel). In the spherically symmetric atmosphere (middle panel), the increase in refractivity error is significantly less pronounced. Above 7 km, the error profiles are quite smooth. There is a small negative bias of about 0.1%, standard deviations under horizontal variability

(spherical symmetry) increase from ~0.2% (<0.1%) at 20 km to ~0.4% (~0.1%) at 7 km.

Below 7 km there is considerable structure in the error profiles. In the spherically symmetric atmosphere, standard deviations reach maximum values of 0.7% at heights around 1.5 km, with a maximum (negative) bias of 0.3%. In the realistic atmosphere, standard deviations reach a maximum value of 1.8% at 1.8 km height, the bias slightly exceeds 0.5% around 2.5 km and below 1.7 km.

3.2. Dependence on the geometry of reference profiles

According to Fig. 4 (bottom panel), differences between "true" vertical profiles at mean tangent point locations and "true" ones along actual 3D tangent point trajectories are very small in the lower stratosphere, since the EGOPS mean location estimate is designed to fit best around 15 km. Below 7 km, however, the differences are of a magnitude comparable to the errors estimated under horizontal variability (top panel). This implies that the geometrical mis-alignment of the actual tangent point trajectory with the mean-vertical contributes as a major source to horizontal variability error. Additional visual evidence for this is that the bias below 7 km in the lower panel appears roughly mirror-symmetric relative to the one in the upper panel. This occurs since the geometrical mis-alignment is a main bias source in both cases so that a clearly visible effect left is the change in sign due to the upper panel using the mean-vertical profile as reference while the lower panel uses the along-trajectory one.

This finding applies also to the other parameters (Figs. 5–7) and indicates the importance of utilizing tropospheric RO profiles not just vertically but as good as possible consistent with the actual tangent point trajectory (or, more generally, occultation plane movement). Overall, the results show that the performance in the realistic horizontally variable troposphere is markedly improved if measured against the actual tangent point trajectory.

3.3. Pressure errors

The pressure errors (Fig. 5) display a similar behavior as the refractivity errors, though the smaller-vertical-scale variations are less pronounced due to the hydrostatic integration.

In the spherical symmetry case, all relative errors increase with decreasing height (bias from 0.1% to 0.2%, standard deviation from 0.2% to 0.34%). In the realistic atmosphere with horizontal variability, standard deviations are smallest around 13 km height (0.2%), below they increase up to ~0.5% around 1.3 km height, where the negative bias also has its maximum value of ~0.2%.

3.4. Geopotential height errors

Errors in the geopotential height of pressure surfaces are shown in Fig. 6 as function of pressure height z_p (a convenient pressure coordinate defined as $z_p = -7 \cdot \ln p$ [hPa]/1013.25), which is closely aligned with height z). Mirroring the pressure errors (see, e.g., Syndergaard, 1999, on the relation between pressure and geopotential height), positive biases in geopotential height correspond to negative biases in pressure (cf. Figs. 5 and 6).

In the realistic atmosphere, biases are <5 gpm above about 7 km, exceed 10 gpm below about 3 km, and reach a maximum of ~13 gpm at ~1.3 km pressure height (corresponding to a pressure error of ~0.2%). Standard deviations are <15 gpm above about 5 km and reach ~33 gpm at lowest levels. In the spherically symmetric atmosphere, the bias above about 7 km is largely the same as in the realistic case, but remains <8 gpm lower down (compared to ~13 gpm with horizontal variability); the standard deviation reaches ~20 gpm (instead of ~33 gpm) at lowest levels.

3.5. Temperature errors

The dry temperature errors are depicted in Fig. 7. In the scenario with horizontal variability, all errors below 7 km are larger than the corresponding errors under spherical symmetry. A positive bias of ~1 K is reached around 2.6, 1.5, and 1.2 km, respectively, where standard deviations of about 4 K are encountered.

Under spherical symmetry, the maximum bias is 0.4 K at 1.2 km, standard deviations remain smaller than 1.2 K. Between 7 and 20 km there is essentially no temperature bias in both scenarios (i.e., always smaller than 0.1 K).

4. Sensitivity to the angle-of-incidence

In this part of the study, the sensitivity of retrieval products to the angle-of-incidence of occultation rays relative to the boresight direction of the receiving antenna (aligned with the LEO orbit plane) is analyzed. Error analyses have been performed for each azimuth sector (ensembles of 20 events), for every atmospheric parameter under study. Occultation events in the 0–10° sector are associated with almost co-planar GNSS and LEO satellites, which should lead to the most-vertical and best-quality occultation events.

Errors in refractivity and pressure, respectively, are—as in Section 3—displayed as relative values in units [%], geopotential height and dry temperature errors as absolute values in units [gpm] and [K], respectively. All statistics are shown between 1 and 20 km above the (ellipsoidal) surface; the dashed vertical lines indicate

relative errors of 0.5% and absolute errors of 10 gpm and 1 K, respectively.

Each of the following figures, Figs. 8–11, shows the results for sector 1 in the top panel, for sector 2 in the middle panel, and for sector 3 in the bottom panel, respectively (the three sectors are defined as described in Section 2.1). Refractivity errors are shown in Fig. 8, pressure errors in Fig. 9, geopotential height errors in

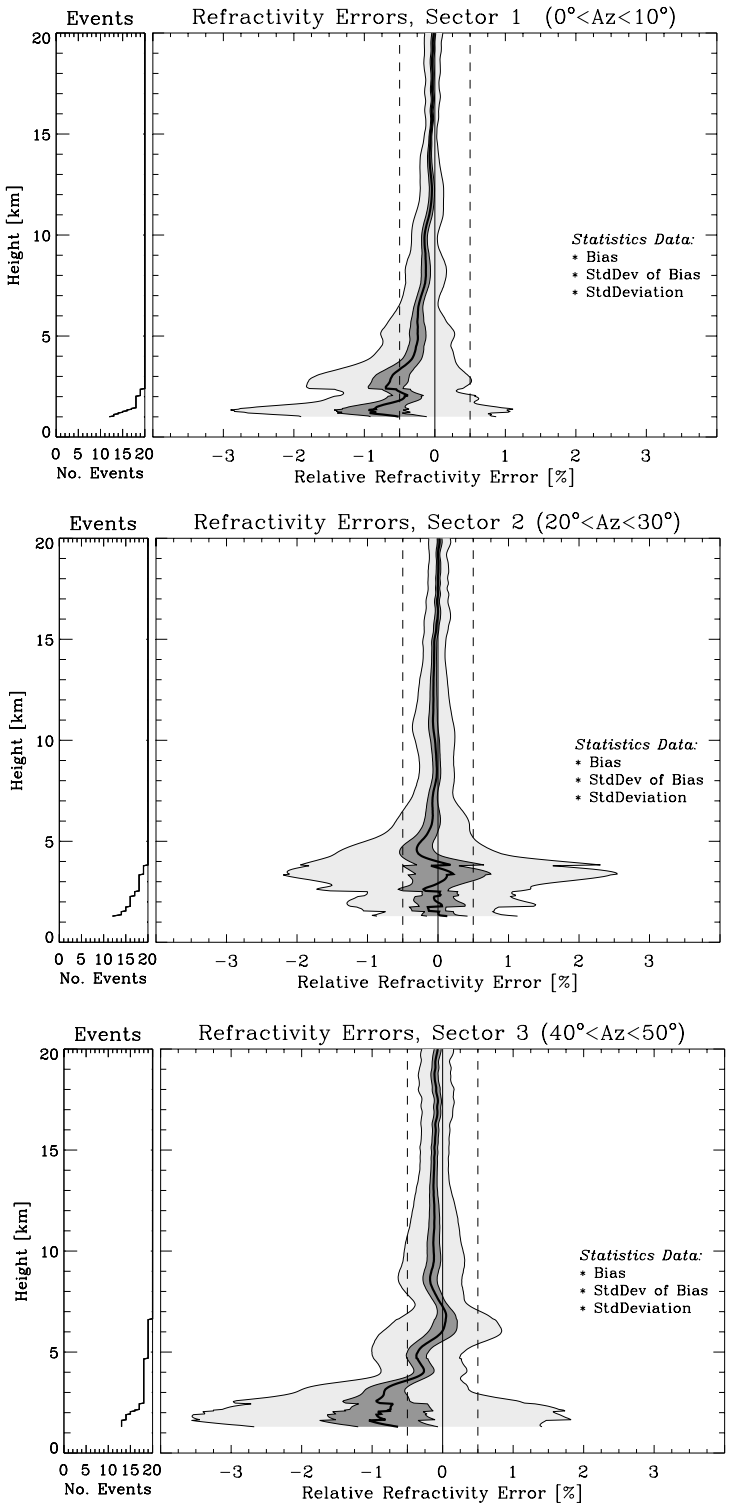

Fig. 8. Refractivity error statistics for occultation events in sector 1 (top panel), sector 2 (mid panel), and sector 3 (bottom panel), respectively.

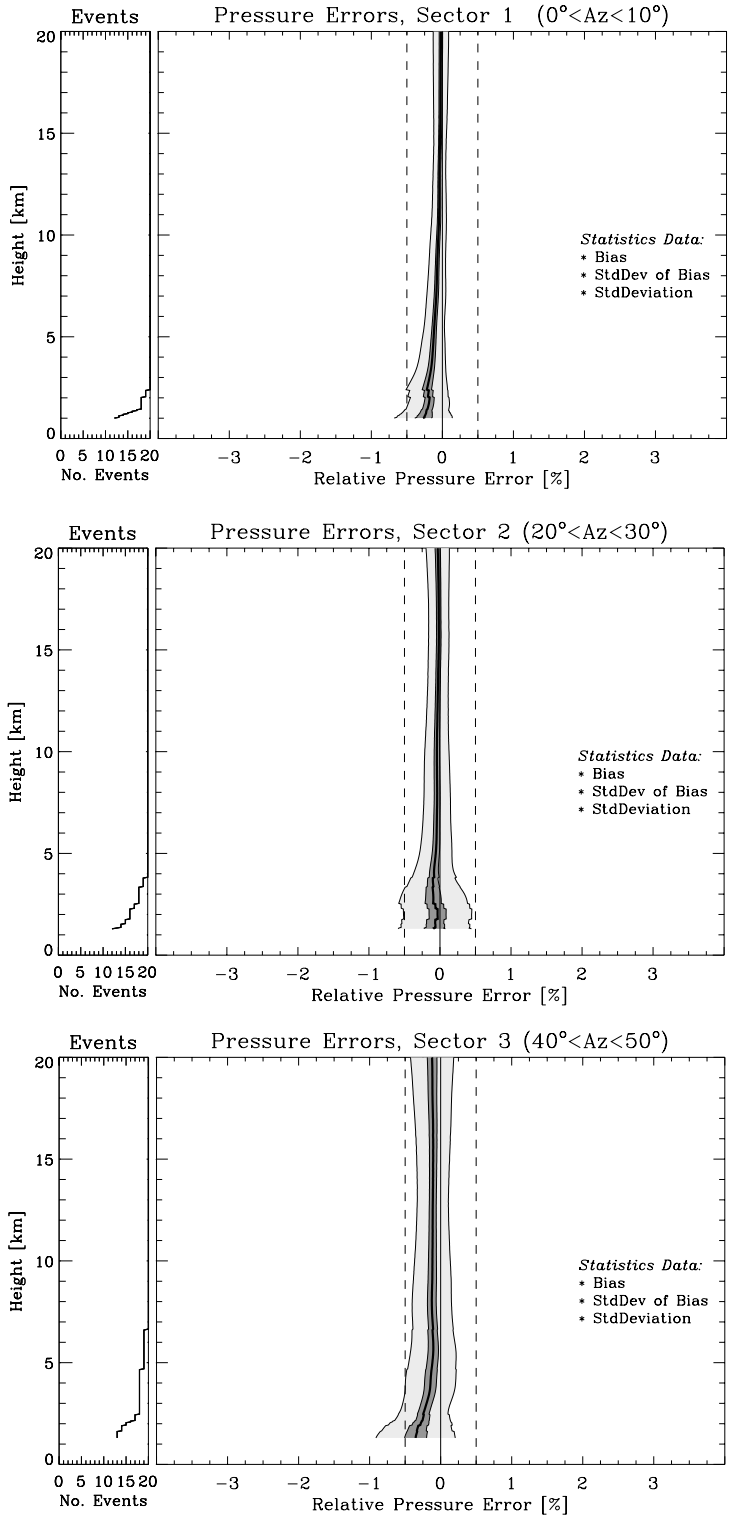

Fig. 9. Pressure error statistics for occultation events in sector 1 (top panel), sector 2 (mid panel), and sector 3 (bottom panel), respectively.

Fig. 10, and dry temperature errors in Fig. 11, respectively.

One general result pertains to all parameters studied: above ~5 to 10 km, the behavior of the result profiles for all parameters is quite similar in that errors increase with increasing angle-of-incidence. Below these heights this is only valid with several exceptions, which deserve further investigation.

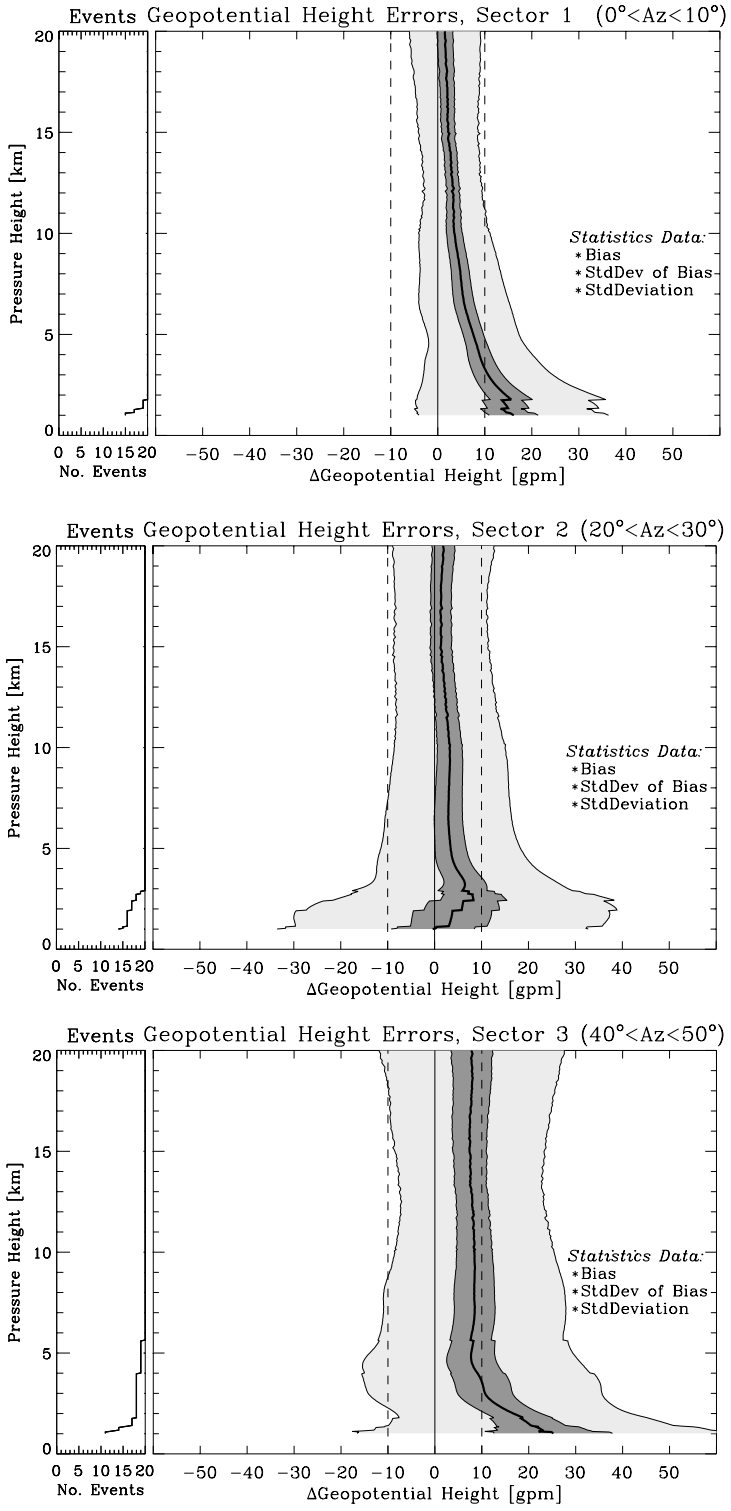

Fig. 10. Geopotential height error statistics for occultation events in sector 1 (top panel), sector 2 (mid panel), and sector 3 (bottom panel), respectively.

4.1. Refractivity errors

The ensemble of 20 occultation events with small angles-of-incidence (sector 1) has no significant bias (less than 0.1%) above 10 km height. Standard deviations in the same height interval are smaller than 0.2%. Between 10 and 2.5 km, bias and standard deviation increase almost continuously (with decreasing height) to 0.7% and 1.1%, respectively. Below ~2.5 km, the increase is less uniform. At ~1.3 km height bias and standard

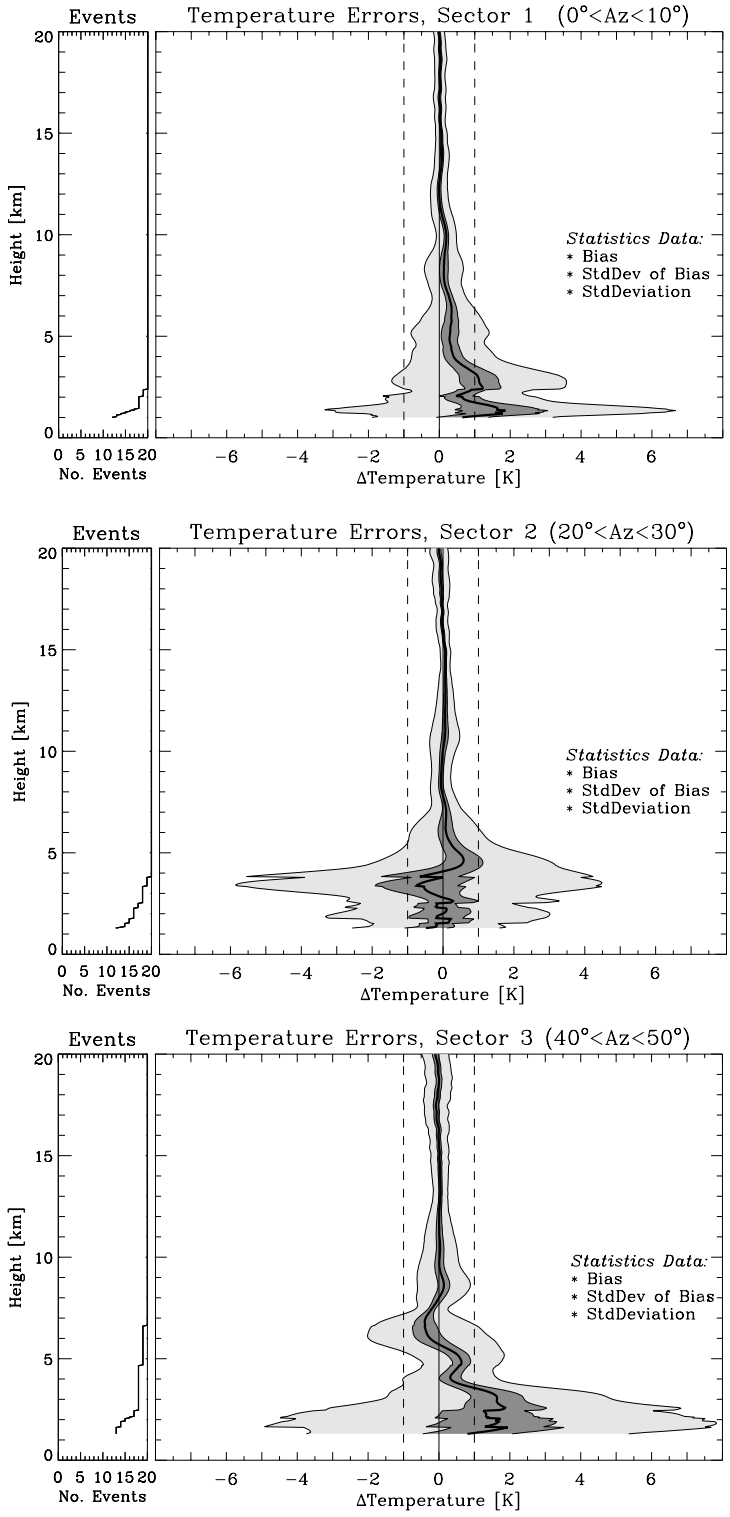

Fig. 11. Temperature error statistics for occultation events in sector 1 (top panel), sector 2 (mid panel), and sector 3 (bottom panel), respectively.

deviation reach maximum values of 0.9% and ~2%, respectively.

Events in sector 2 show remarkable features in the height interval below 10 km: the bias is explicitly smaller than in sector 1, while standard deviations are of comparable size (maximum: ~2.3% near 3.5 km). At 4.5 km, the bias reaches a maximum (negative) value of −0.3%, below that it oscillates around zero. Below 3.5 km, the error estimates become smaller again, which roots partly in the fact that the sample size decreases gradually (see

left-hand side subpanel of middle panel of Fig. 8) leaving a smaller ensemble tentatively composed of more "well-behaved" profiles.

Events with angles-of-incidence between 40° and 50° (sector 3) exhibit an approximately constant negative bias of about 0.1% above 8 km height, while standard deviations are markedly larger. The largest biases (near 1%) and standard deviations (~2.5%) are encountered at around 1.5–2 km height.

4.2. Pressure errors

All sectors display (generally very small) negative biases over the entire height domain. Standard deviation are smaller than 0.5% almost everywhere; they are smallest in sector 1, whereas biases are smallest in sector 2.

Occultation events in sector 1 exhibit biases of less than 0.1% between 6 and 20 km, which are, nevertheless, slightly larger than corresponding biases in sector 2. Below 6 km, they gradually increase to ~0.2% at lowest levels. Standard deviations remain smaller than 0.4% at all heights.

Events in sector 2 have the smallest biases in the entire height domain: they are always smaller than ~0.1%. Standard deviations remain almost constant (about 0.2%) down to about 10 km, then they start to increase gradually but never exceed 0.5%.

Events in sector 3 display a marked (constant) negative bias of ~0.1% between 5 and 20 km height, while standard deviations amount to about 0.2% (approximately constant as well). Below 5 km, the bias increases continuously to ~0.4%. Standard deviation increase to ~0.6% at lowest levels.

4.3. Geopotential height errors

Geopotential height errors are, as already in Fig. 6 of Section 3, displayed as functions of pressure height. Positive biases (related to negative pressure biases) can be detected in all sectors. In line with the pressure error results they are smallest in sector 2, while standard deviations are smallest in sector 1.

The bias in sector 1 increases continuously from ~1.5 gpm at 20 km to 16 gpm at 1 km pressure height, the standard deviations from ~7.5 to ~20 gpm.

Sector 2 has again the smallest bias, the maximum is slightly more than 8 gpm near 2.5 km. Standard deviations grow evenly from ~10 gpm at 20 km to ~33 gpm at 1 km.

In sector 3, there is a pronounced positive bias of about 8 gpm between 20 and 4 km, which increases downwards to about 25 gpm. Standard deviations rise from about 20 gpm at 20 km to about 40 gpm at 1 km.

4.4. Temperature errors

The temperature errors (Fig. 11) closely reflect the overall behavior of the refractivity errors (Fig. 8), though with a change in sign leading to mirror-symmetry of temperature vs. refractivity errors. This behavior is caused by the inverse relation of the two parameters via the equation of state and was explored in detail by Rieder and Kirchengast (2001a,b).

Events in sector 1 exhibit very small biases of less than ~0.1 K above 10 km, which slowly (but not uniformly) increase to 0.4 K at 4 km and come close to 2 K at lowest levels. Standard deviations increase from ~0.2 K at 20 km to ~2.5 K at near 3 km.

Events in sector 2 are practically bias-free between 6 and 20 km (biases <0.1 K). Below this height, biases remain <0.8 K throughout. Standard deviations in this lower height domain are only slightly larger than in sector 1.

Events in sector 3, finally, show small biases, never exceeding 0.1 K, down to about 9 km. Below 4 km, biases increase markedly and reach a maximum value of close to 2 K at 2.5 km. Standard deviations are around 0.5 K down to 10 km. Below 4 km, there is a pronounced increase of up to ~6 K between 1.5 and 2 km height.

5. Summary, conclusions, and outlook

This study addressed the sensitivity of GNSS RO measurements to atmospheric horizontal variability. Retrieved geophysical parameters from refractivity via pressure and geopotential height to dry temperature have been investigated.

The errors in a realistic horizontally variable atmosphere have been compared with errors in a spherically symmetric atmosphere. This investigation was based on an ensemble of 60 simulated occultations, using a representative ECMWF T213L50 analysis field with and without horizontal variability, respectively. Below ~7 km height biases and standard deviations of all considered atmospheric parameters under spherical symmetry are significantly smaller than corresponding errors in a realistic atmosphere with horizontal variability. Temperature standard deviations below 5 km, for example, remain smaller than 1.2 K in a spherically symmetric atmosphere while they reach values of about 4 K in the realistic atmosphere. This confirms earlier results based on a more simplified estimation by Kursinski et al. (1997), that horizontal variability is an important error source in the troposphere. Dry temperature profiles between 7 and 20 km were found to be essentially bias-free in both the realistic and spherical-symmetry scenarios (biases smaller than 0.1 K), which confirms the unique climate monitoring utility of GNSS occultation

data. Small residual biases of ~0.2–0.3 K between about 7 and 14 km where found, though, for ensembles of events at high latitudes within separate parallel work (Foelsche et al., 2003). Within this study, involving only about 10 events at high latitudes (poleward of 60°), that residual bias was (partly) visible only in the results for the 0–10° azimuth sector. Nevertheless, it certainly calls for closer study in the future.

A significant part of the total error below ~7 km can be attributed to adopting reference profiles vertically at mean tangent point locations (designed to fit best at heights around 15 km) instead of extracting them along actual 3D tangent point trajectories through the troposphere. This finding indicates the importance of utilizing tropospheric RO profiles as good as possible consistent with the actual tangent point trajectory (or, more generally, occultation plane movement). Future work will investigate this matter more closely based on a larger ensemble of events and on an even higher-resolved field (ECMWF T511L60 analysis field). We will also rigorously inspect by how much the standard deviation and bias errors decrease if the data are exploited along a tangent point trajectory deduced purely from observed data, mainly GNSS and LEO satellite position and bending angle data.

The sensitivity of retrieval products to the angle-of-incidence of occultation rays relative to the boresight direction of the receiving antenna was analyzed for three different azimuth sectors. Below about 7 km, the general result for all parameters studied is qualitatively quite clear: most errors were found to increase with increasing angle of incidence. This is in line with the hypothesis that larger angles of incidence lead to more sensitivity to horizontal variability. Biases in the 20–30° azimuth sector are generally smaller than corresponding biases in the 0–10° sector, however, despite the latter is associated with almost co-planar GNSS and LEO satellites, which should lead to the most-vertical and best-quality occultation events. This may be due to the comparatively small number of occultation events in the present study but certainly merits further investigation. In general, the sensitivity of bias errors to increases of the angle of incidence has been found to be relatively small, which is favorable regarding the climate monitoring utility of the data. For example, dry temperature biases between 7 and 20 km exhibit no relevant increase with increasing angle of incidence. Current cautionary approaches restricting the events used in climate studies to small angles of incidence (such as <15°; Steiner et al., 2001) may thus be overly conservative.

Future work needs to further improve the understanding of all errors involved, in particular of the residual biases, in order to eliminate or mitigate them to the largest extend possible. This will optimize the climatological quality of the data at all angles of incidence.

Acknowledgements

The authors thank A.K. Steiner (IGAM/UG) and S. Syndergaard (University of Arizona, Tucson, USA) for support in preparing some auxiliary computer codes used in the study. The EGOPS software, the core tool of the study, was developed by an international consortium led by IGAM/UG and involving partner teams at Danish Meteorological Institute and TERMA Elektronik A/S, Denmark, the Meteorological Office, UK, and Austrian Aerospace GmbH, Austria, with the major funding provided by the European Space Agency. The European Centre for Medium-Range Weather Forecasts (ECMWF, Reading, UK) provided the atmospheric analysis field used. The study was funded by the European Space Agency under ESA/ESTEC Contract No. 14809/00/NL/MM. Furthermore, U.F. received financial support for the work from the START research award of G.K. funded by the Austrian Ministry for Education, Science, and Culture and managed under Program No. Y103-CHE of the Austrian Science Fund.

References

Ahmad, B., Tyler, G.L., 1999. Systematic errors in atmospheric profiles obtained from Abelian inversion of radio occultation data: effect of large-scale horizontal gradients. J. Geophys. Res. 104 (D4), 3971–3992.

Foelsche, U., Kirchengast, G., Steiner, A.K., 2003. Global climate monitoring based on CHAMP/GPS radio occultation data. In: Reigber, et al. (Eds.), First CHAMP Mission Results for Gravity Magnetic and Atmospheric Studies. Springer, Berlin.

Gobiet, A., Kirchengast, G., 2002. Sensitivity of atmospheric profiles retrieved from GNSS occultation data to ionospheric residual and high-altitude initialization errors. Technical Report for ESA/ESTEC No. 1/2002, Institute for Geophysics, Astrophysics, and Meteorology, University of Graz, Austria.

GRAS-SAG, 1998. The GRAS instrument on METOP, ESA/EUMETSAT Report (ESA No. VR/3021 /PI, EUM.No. EPS/MIS/IN/9), ESA/ESTEC, Noordwijk, Netherlands, 38p.

Healy, S.B., 2001. Radio occultation bending angle and impact parameter errors caused by horizontal refractivity index gradients in the troposphere: a simulation study. J. Geophys. Res. 106 (D11), 11,875–11,889.

Hedin, A.E., 1991. Extension of the MSIS thermosphere model into the middle and lower atmosphere. J. Geophys. Res. 96, 1159–1172.

Kahle, H.-G., 1984. Reference ellipsoid and geoid. In: Fuchs, K., Stoffel, H. (Eds.), Landolt-Börnstein Numerical Data and Functional Relationships in Science and Technology. Springer-Verlag, Berlin. Volume 2, Subvolume A, pp. 332–336.

Kirchengast, G., 1998. End-to-end GNSS Occultation Performance Simulator overview and exemplary applications, Wissenschaft. Ber. No. 2/1998, Institute for Meteorology and Geophysics, University of Graz, Austria.

Kirchengast, G., Fritzer, J., Ramsauer, J., 2001. End-to-end GNSS Occultation Performance Simulator Version 4 (EGOPS4) Software User Manual (Overview and Reference Manual), Technical Report for ESA/ESTEC No. 5/2001, Institute for Geophysics, Astrophysics, and Meteorology, University of Graz, Austria, Available from

<http://www.uni-graz.at/igam-arsclisys/ARSCliSys_papers_en.html>.

Kursinski, E.R., Hajj, G.A., Schofield, J.T., Linfield, R.P., Hardy, K.R., 1997. Observing earth's atmosphere with radio occultation measurements using the Global Positioning System. J. Geophys. Res. 102 (D19), 23429–23465.

Rieder, M.J., Kirchengast, G., 2001a. Error analysis for mesospheric temperature profiling by absorptive occultation sensors. Ann. Geophys. 19, 71–81.

Rieder, M.J., Kirchengast, G., 2001b. Error analysis and characterization of atmospheric profiles retrieved from GNSS occultation data. J. Geophys. Res. 106, 31,755–31,770.

Salby, M.L., 1996. Fundamentals of Atmospheric Physics. Academic Press, San Diego.

Smith, E.K., Weintraub, S., 1953. The constants in the equation for atmospheric refractive index at radio frequencies. Proc. IRE 41, 1035–1037.

Steiner, A.K., Kirchengast, G., Ladreiter, H.P., 1999. Inversion, error analysis and validation of GPS/MET occultation data. Ann. Geophys. 17, 122–138.

Steiner, A.K., Kirchengast, G., Foelsche, U., Kornblueh, L., Manzini, E., Bengtsson, L., 2001. GNSS occultation sounding for climate monitoring. Phys. Chem. Earth (A) 26, 113–124.

Syndergaard, S., 1999. Retrieval analysis and methodologies in atmospheric limb sounding using the GNSS radio occultation technique. DMI Scient. Report 99-6. Danish Meteorological Institute, Copenhagen, Denmark, 131p.